*J Mater Sci*

**Ceramics**

# Bond analysis of novel $MnZrTa_2O_8$ microwave dielectric ceramics with monoclinic structure

Yun Zhang[1,*], Shihua Ding[1], Chao Li[1], Tianxiu Song[1], and Yingchun Zhang[2]

[1] *School of Materials Science and Engineering, Xihua University, Chengdu 610039, China*
[2] *School of Materials Science and Engineering, University of Science and Technology Beijing, Beijing 100083, China*

**Received:** 18 January 2020
**Accepted:** 30 March 2020

## ABSTRACT

A new type of ceramic, namely $MnZrTa_2O_8$, was synthesized after sintering at high temperature in this work. The possible dielectric loss mechanism was discussed by Raman spectroscopy and chemical bond theory. X-ray diffraction indicated that $MnZrTa_2O_8$ formed through a reaction between $ZrO_2$ and intermediate $MnTa_2O_6$. After sintering at 1350 °C, a monoclinic structure with cell parameters $a$ = 4.8370(3) Å, $b$ = 5.7163(1) Å, $c$ = 5.1398(5) Å, $\beta$ = 91.7219° was gained for ceramic. Among all bonds, Ta–O with the greatest bond ionicity and lattice energy was the dominant factor that influenced the microwave dielectric properties. The temperature coefficient of the resonant frequency $\tau_f$ changed from − 50.55 to − 41.21 ppm/ °C, which was related to the lattice energy. The effect of porosity on dielectric loss was also checked and found to be significant. $MnZrTa_2O_8$ ceramic exhibited relative permittivity $\varepsilon_r \sim 23.0$ and enhanced quality factor $Q \times f \sim 48103$ GHz (at 8.97 GHz), which provided a promising candidate for electric components.

## Introduction

The rapid development of 5G wireless communication has resulted in an increasing demand for microwave dielectric ceramics. The crucial characteristics for resonators are (1) suitable range of dielectric constant ($\varepsilon_r$), (2) excellent quality factor ($Q \times f$, $Q$ is subjected to dielectric loss tan$\delta$) to determine frequency selectivity and (3) near zero temperature coefficient of the resonant frequency ($\tau_f$ = 0±5 ppm/ °C) for frequency stabilization [1–3]. Particularly, relative permittivity $\varepsilon_r$ should be in the range of 20–50 in cell phone base stations [4]. While $Ba(Mg_{1/3}Ta_{2/3})O_3$ has superior dielectric properties and is widely used as microwave device, it often needs high processing temperature (~ 1600 °C) [5]. The search for new types of dielectrics has become more imperative than ever.

$AZrNb_2O_8$ (A: Co, Mg, Zn and Mn) materials featured $\varepsilon_r$ of 9.6–16.5 and $Q \times f$ of 26950–58500 GHz, turning out to be attractive candidates for microwave applications [6]. The variations in $Q \times f$ and $\varepsilon_r$ were explained on the basis of packing fraction and ionic polarizability, respectively [6]. For the purpose of

---

Address correspondence to E-mail: yunzhang_17@163.com

https://doi.org/10.1007/s10853-020-04629-z

achieving bulk ceramics at relatively low temperature, 3 wt% $BaCu(B_2O_5)$ was added into $ZnZrNb_2O_8$ [7]. The same result was obtained by an aqueous sol–gel technique, since nano-sized particles usually possessed high surface area [8]. Specifically for $NiZrNb_2O_8$, its $\tau_f$ and $Q \times f$ were improved with the help of $ZnTa_2O_6$ [9].

Due to the similar effective ionic radii of Nb and Ta, researchers paid much attention to ion substitution. Li [10, 11] designed and fabricated ultra-low-loss $AZrTa_2O_8$ (A = Mg, Zn) with $Q \times f$ up to 110700–140900 GHz. More importantly, the $Q \times f'$ for $Mg_{0.9}Ca_{0.1}ZrTa_2O_8$ had more than doubled, presenting the highest level among current wolframite dielectrics [12]. Recently, we have carried out a systematic study about Ta-doped $NiZrNb_2O_8$. The $Q \times f$ was considerably increased to 86404 GHz, and the large $\tau_f$ was compensated by adjusting chemical composition [13]. The scientific reports indicated that Ta substitution for Nb might be effective in optimizing the dielectric properties of $AZrNb_2O_8$ ceramics. Problems, however, remained in explaining the dielectric loss mechanism under microwave field.

$MnZrNb_2O_8$, a member of $AZrNb_2O_8$ family, exhibited $Q \times f$ 27936 GHz [6]. Thus, an improvement would be worth investigating. On the other hand, many novel Ta-based materials, such as $NiSnTa_2O_8$ [14], $MgTiTa_2O_8$ [15] and $Co_{0.5}Ti_{0.5}TaO_4$ [16] were reported to have interesting properties, indicating their potential applications in microwave communication technology. All these factors promoted us to search for low-loss $MnZrTa_2O_8$ system. As already mentioned, the microwave property was particularly susceptible to crystal structure and more specifically the chemical bonds. Nevertheless, to the best of our knowledge, there are few studies about the bond characteristic investigations of $AZrTa_2O_8$ ceramics. Therefore, we also make an effort to explore the structure–properties relationships based on Phillips–Van Vechten–Levine (P–V–L) bond theory.

## Experimental procedures

$MnZrTa_2O_8$ ceramic was prepared by solid-state reaction technique. Raw reagents of MnO (99.5%), $ZrO_2$ (99%) and $Ta_2O_5$ (99.5%) were purchased from Aladdin (Shanghai, China). They were ball-milled for 6 h with desired stoichiometry. The slurry was then dried, manually ground in a mortar and sieved through a 200-mesh screen. Initial calcination was carried out at 1125–1200 °C to ensure complete chemical reaction. After that, the samples were reground in ethanol medium. Using polyvinyl alcohol (PVA) as binder, the spherical powders were isostatically pressed into disks at 150 MPa. Finally, the compacts were sintered at 1300–1400 °C for 4 h in air atmosphere.

The bulk densities of sintered pellets were measured by Archimedes principle. The theoretical density was calculated by formula:

$$\rho_{\text{theory}} = \frac{ZA}{V_C N_A} \quad (1)$$

where $Z$, $A$, $V_C$ and $N_A$ were the number of atoms in a unit cell, the atomic weight, the volume of the unite cell and Avogadro's number, respectively. Constituent phases were examined by X-ray diffraction (XRD, D2-PHASER, Bruker) with Cu$K\alpha$ radiation. The structural parameters of samples were refined by means of GSAS software [17]. The Raman spectrum was collected using Renishaw RM2000 instrument. And the exciting source was 532 nm line from Ar ion laser. Field emission scanning electron microscope (ZEISS GeminiSEM 300, Carl Zeiss, Germany) was employed to observe the morphology. The dielectric constant $\varepsilon_r$ and quality factor $Q \times f$ were measured in the frequency range of 7–10 GHz with a HP8720ES network analyzer using Hakki–Coleman's dielectric resonator method [18]. The $\tau_f$ was obtained at temperatures from 20 to 80 °C as the relationship:

$$\tau_f = \frac{f_2 - f_1}{f_1(T_2 - T_1)} \quad (2)$$

where $f_1$ and $f_2$ were the resonant frequency at $T_1$ and $T_2$, respectively.

## Results and discussion

### Relative density

The bulk density of $MnZrTa_2O_8$ ceramic sintered at various temperatures is demonstrated in Fig. 1. From the preliminary result, it was evident that the bulk density enlarged monotonically with increasing temperature up to 1350 °C, and decreased thereafter. The dependence of relative density on sintering temperature illustrated a similar trend to that of bulk density, as shown in Fig. 1. Sintered at 1350 °C, the

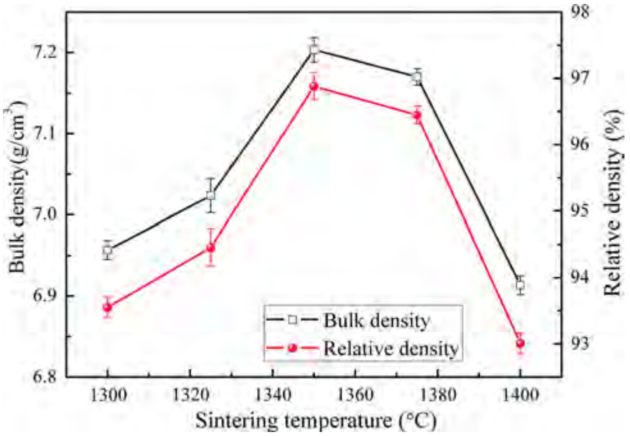

**Figure 1** Sintering behavior of $MnZrTa_2O_8$ ceramics at different temperatures.

ceramic reached the maximum relative density ~96.85%.

## Structure analysis and phase refinement

Figure 2a reports the XRD patterns of powders calcined in the temperature range 1125–1200 °C. Major crystalline phase $MnZrTa_2O_8$ as well as a low level of unfavorable starting oxides could be identified at 1125 °C. Minor $MnTa_2O_6$ phase was also detected, matching JCPDS 34-0054. It became clear that increasing temperature gradually weakened the intensities of $MnTa_2O_6$ reflections. Monophasic $MnZrTa_2O_8$ was obtained at 1200 °C. The above discussion briefly indicated the transition from $MnTa_2O_6$ to $MnZrTa_2O_8$, as illustrated by Eqs. (3) and (4). This phenomenon was almost the same as generally observed in $CoO–ZrO_2–Ta_2O_5$ system [13]. After sintering, the obtained compound was virtually phase pure, according to JCPDS file number 48-0331 (in Fig. 2b).

$$MnO + Ta_2O_5 = MnTa_2O_6 \tag{3}$$

$$MnTa_2O_6 + ZrO_2 = MnZrTa_2O_8 \tag{4}$$

GSAS-EXPGUI software was performed to obtain precise structure parameters. The refinement plot and atomic fractional coordinates for $MnZrTa_2O_8$ ceramic sintered at 1350 °C are shown in Fig. 3 and Table 1, respectively. Judging from the reliability factors in Table 2, the refinements could be originally used to determine structure–properties relationships. Figure 4 and Table 3 summarize the structural diagram, bond type and bond length. In $MnZrTa_2O_8$, Mn/Zr was randomly distributed at 2*f* Wyckoff positions, and Ta was in 2*e*. Two types of O anions, both located at 4*g* sites, were distinguished. O1 was connected to one Ta cation and two Mn/Zr cations, while O2 was bonded with one Mn/Zr-site and two Ta-site cations. All cations were 6-coordinated, forming oxygen octahedrons in sequence. Surrounded by $Mn/ZrO_6$ with vertices, $TaO_6$ was inter-connected through edge-sharing [19].

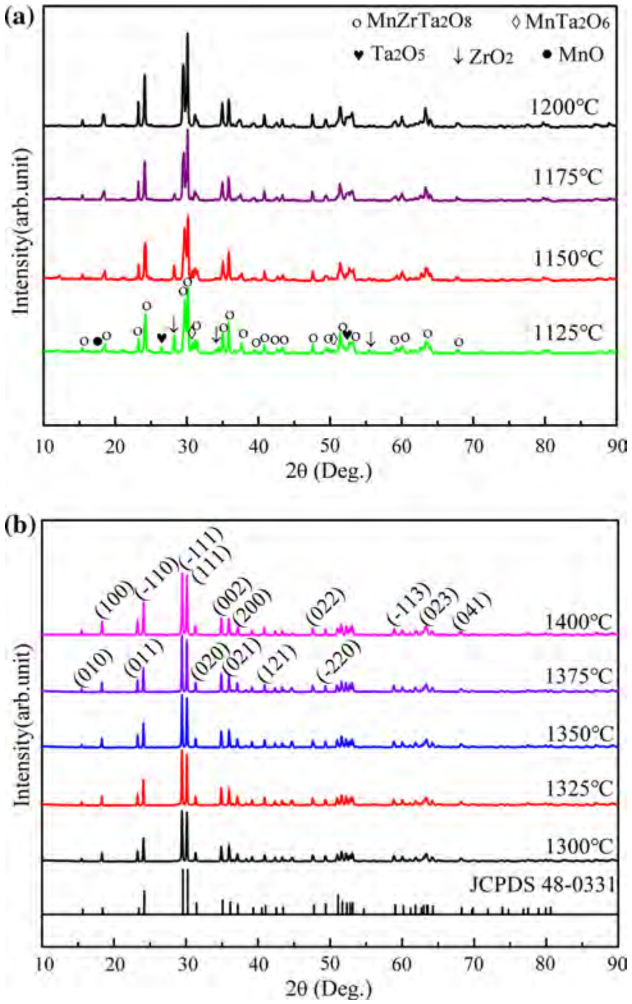

**Figure 2** XRD patterns of $MnZrTa_2O_8$ samples **a** calcined at 1125–1200 °C and **b** sintered at 1300–1400 °C.

## Raman analysis

Raman spectroscopy is introduced with the aim of probing the crystal structure in this work. For $MnZrTa_2O_8$ with $P2/c$ space group and $C_{2h}$ (2/m) point group, its irreducible representations are determined as given in Table 4 [20]. Considering that

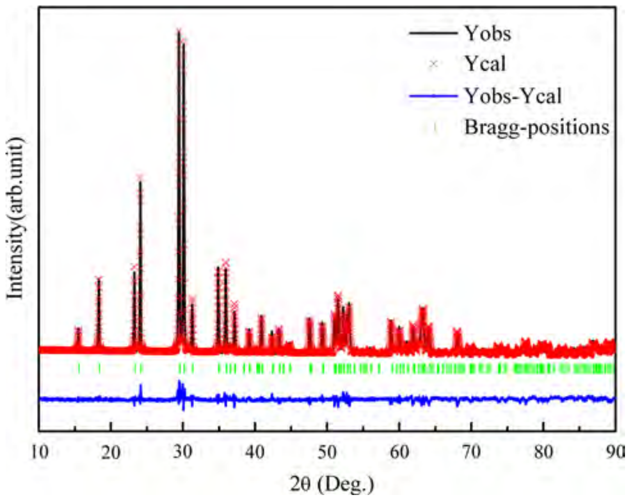

**Figure 3** Rietveld refinement details of $MnZrTa_2O_8$ samples sintered at 1350 °C.

**Table 1** Refined atomic fractional coordinates from the XRD data for $MnZrTa_2O_8$

| Atom | Wyckoff site | *x* | *y* | *z* | OCC |
|---|---|---|---|---|---|
| Mn | 2*f* | 0.5000 | 0.6820 | 0.2500 | 0.5 |
| Zr | 2*f* | 0.5000 | 0.6794 | 0.2500 | 0.5 |
| O1 | 4*g* | 0.2481 | 0.3746 | 0.3838 | 1 |
| O2 | 4*g* | 0.2090 | 0.0979 | 0.9567 | 1 |
| Ta | 2*e* | 0.0000 | 0.1753 | 0.2500 | 1 |

some weak vibration modes may be broadened or overlapped, less bands are recorded as shown in Fig. 5. For lattice vibration, the weak bands were centered at 117 $cm^{-1}$ and 154 $cm^{-1}$ [9]. The Zr–O stretching vibrations at 175 $cm^{-1}$, 412 $cm^{-1}$, and 835 $cm^{-1}$ were readily recognized [21]. O–Ta–O bending modes appeared at low wavenumbers (200–300 $cm^{-1}$). The spectral maxima were mainly located at 800–1000 $cm^{-1}$. The strong structures at 850 $cm^{-1}$ and 739 $cm^{-1}$ were consistent with the Ta–O symmetric stretching vibration, which were represented as $A_{3g}$ and $B_{3g}$ modes, respectively [9]. The 482 $cm^{-1}$ and 679 $cm^{-1}$ peaks also gave information about Ta–O stretching. Two extra active phonons near 799 $cm^{-1}$ and 879 $cm^{-1}$ originated from the stretch vibration of the $TaO_6$ octahedra [22]. The modes at 522 $cm^{-1}$, 626 $cm^{-1}$ and 647 $cm^{-1}$ might be viewed as the symmetric stretching vibration $v_2$(Mn–O) [23, 24], whereas the peak in the vicinity of 579 $cm^{-1}$ belonged to $MnO_6$ bending. Besides, the $B_{3g}$ mode near 363 $cm^{-1}$ came from the rotations of $MnO_6$ groups. [23].

## Morphological analysis

SEM images of $MnZrTa_2O_8$ ceramics are presented in Fig. 6. The difference in microstructure was clearly seen in terms of grain size and porosity. The sintering was incomplete when the temperature was as low as 1300 °C. Here, the microstructure was represented by a proportion of intergranular porosity. Grain growth accelerated integrally and porosity reduction occurred as sintering proceeded. These two effects combined to give enhanced microstructure. After sintering at 1350 °C, the faceted morphology was more clearly. Meanwhile, the polygonal grains exhibited dimensions between 1 and 4 μm (see Fig. 6c). However, on further increasing the temperature, uniform microstructure was destroyed. This over-sintering behavior resulted in abnormal grain growth with size up to 8 μm, as shown in Fig. 6e.

## Microwave dielectric properties and bond analysis

Phillips–Van Vechten theory [25, 26] could only deal with the binary crystals at the end of the 1960s. Zhang [27] further succeeded in generalizing Phillips–Van Vechten–Levine (P–V–L) theory for multibond

**Table 2** Crystallographic data obtained from Rietveld refinement for $MnZrTa_2O_8$ ceramics

| *T*(°C) | Lattice parameters | | | | | $V_{unit}$ (Å$^3$) | Reliability factors |
|---|---|---|---|---|---|---|---|
| | *a* (Å) | *b* (Å) | *c* (Å) | *α* = *γ* | *β* | | $R_{wp}$ (%) $R_p$ (%) |
| 1300 | 4.8359(3) | 5.7169(1) | 5.1387(7) | 90 | 91.7224(1) | 142.0049(6) | 9.1, 8.7 |
| 1325 | 4.8361(1) | 5.7164(4) | 5.1395(2) | 90 | 91.7211(4) | 142.0186(4) | 8.9, 7.5 |
| 1350 | 4.8370(3) | 5.7153(5) | 5.1398(5) | 90 | 91.7219(3) | 142.0273(9) | 9.6, 8.3 |
| 1375 | 4.8371(4) | 5.7159(2) | 5.1399(4) | 90 | 91.7209(7) | 142.0480(9) | 9.5, 8.1 |
| 1400 | 4.8369(2) | 5.7177(3) | 5.1391(2) | 90 | 91.7198(6) | 142.0637(7) | 8.6, 7.3 |

$R_{wp}$ reliability factor of weighted pattern; $R_p$ reliability factor of patterns

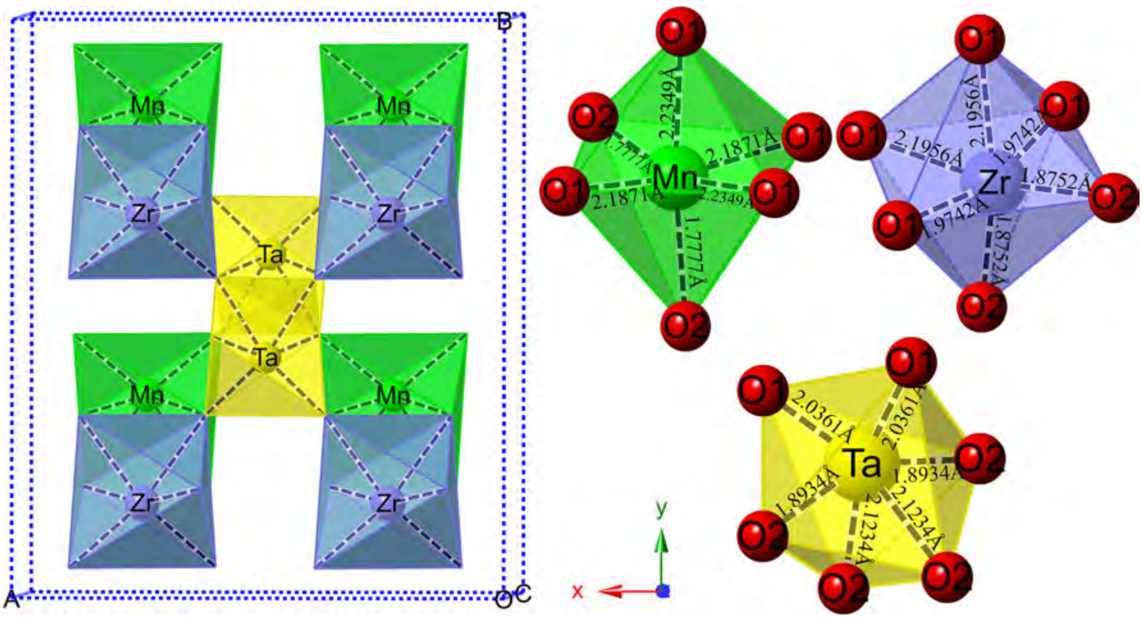

**Figure 4** The schematic diagram of $MnZrTa_2O_8$ ceramics, as well as bond lengths within octahedrons after sintering at 1350 °C.

**Table 3** Bond length (Å) for $MnZrTa_2O_8$ ceramics sintered at various temperatures

| Bond type | 1300 °C | 1325 °C | 1350 °C | 1375 °C | 1400 °C |
|---|---|---|---|---|---|
| Mn–O(1)$^1$ × 2 | 2.1874 | 2.1882 | 2.1871 | 2.1875 | 2.1884 |
| Mn–O(1)$^2$ × 2 | 2.2344 | 2.2351 | 2.2349 | 2.2361 | 2.2370 |
| Mn–O(2) × 2 | 1.7794 | 1.7785 | 1.7777 | 1.7791 | 1.7795 |
| Zr–O(1)$^1$ × 2 | 1.9755 | 1.9759 | 1.9742 | 1.9740 | 1.9772 |
| Zr–O(1)$^2$ × 2 | 2.1954 | 2.1962 | 2.1956 | 2.1955 | 2.1967 |
| Zr–O(2) × 2 | 1.8749 | 1.8744 | 1.8752 | 1.8761 | 1.8754 |
| Ta–O(1) × 2 | 2.0374 | 2.0354 | 2.0361 | 2.0356 | 2.0334 |
| Ta–O(2)$^1$ × 2 | 2.1273 | 2.1254 | 2.1234 | 2.1222 | 2.1304 |
| Ta–O(2)$^2$ × 2 | 1.8927 | 1.8951 | 1.8934 | 1.9012 | 1.9007 |

**Table 4** Raman and IR vibrations modes of $MnZrTa_2O_8$

| Atom | Wyckoff site | Symmetry | Irreducible vibrational representations |
|---|---|---|---|
| Mn/Zr | 2*f* | $C_2$ | $A_g + 2B_g + A_u + 2B_u$ |
| O1 | 4*g* | $C_1$ | $3A_g + 3B_g + 3A_u + 3B_u$ |
| O2 | 4*g* | $C_1$ | $3A_g + 3B_g + 3A_u + 3B_u$ |
| Ta | 2*e* | $C_2$ | $A_g + 2B_g + A_u + 2B_u$ |
| $\Gamma_{Optic} = 9A_g + 12B_g + 8A_u + 10B_u$ | | | |
| $\Gamma_{Raman} = 9A_g + 12B_g$ | | | |
| $\Gamma_{IR} = 8A_u + 10B_u$ | | | |

systems. Using this, any complex crystal could be divided into a sum of dualistic crystal ($A_mB_n$). In $MnZrTa_2O_8$, the effective valence electron numbers ($Z$) of Mn, Zr, Ta were $Z_{Mn} = 2$, $Z_{Zr} = 4$ and $Z_{Ta} = 5$, respectively, while the $Z_O$ values were not equal, depending on the type of bond. They were $Z_O = -1$ in Mn–O bond, $Z_O = -2$ in Zr–O bond and $Z_O = -2.5$ in Ta–O bond. The coordination number and charge distribution of ions are shown in Fig. 7. These parameters were especially necessary for the calculation of bond ionicity $f_i$, lattice energy $U_{cal}$ and bond energy $E$. The $MnZrTa_2O_8$ is decomposed into the sum of binary crystals as Eq. (5).

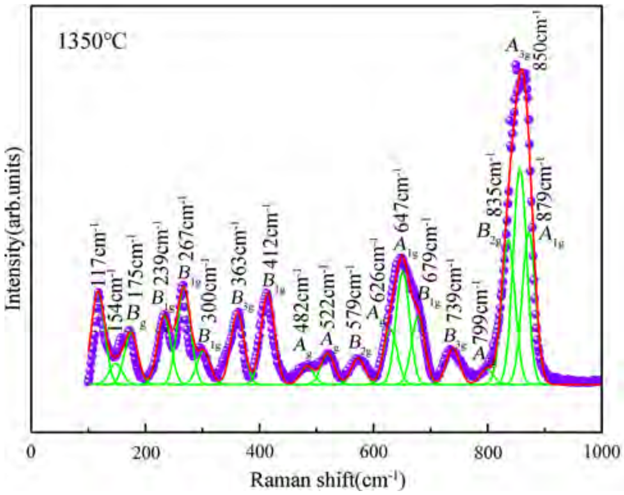

**Figure 5** The Lorentzian peak fit of the experimental Raman profile for $MnZrTa_2O_8$ ceramics sintered at 1350 °C. The symbols are experimental points, and the solid lines are fitted curves.

$$\begin{aligned} MnZrTa_2O_8 &= Mn_{2/3}O(1)_{4/3} + Mn_{1/3}O(2)_{2/3} + Zr_{2/3}O(1)_{4/3} \\ &\quad + Zr_{1/3}O(2)_{2/3} + Ta_{2/3}O(1)_{4/3} + Ta_{4/3}O(2)_{8/3} \\ &= Mn_{1/3}O(1)^{1}_{2/3} + Mn_{1/3}O(1)^{2}_{2/3} + Mn_{1/3}O(2)_{2/3} \\ &\quad + Zr_{1/3}O(1)^{1}_{2/3} + Zr_{1/3}O(1)^{2}_{2/3} + Zr_{1/3}O(2)_{2/3} \\ &\quad + Ta_{2/3}O(1)_{4/3} + Ta_{2/3}O(2)^{1}_{4/3} + Ta_{2/3}O(2)^{2}_{4/3} \end{aligned} \tag{5}$$

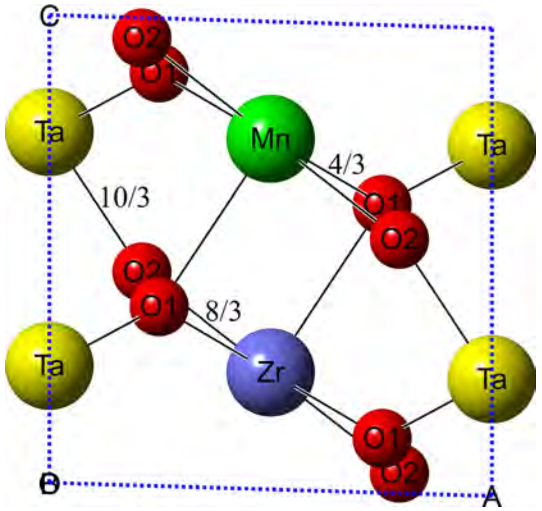

**Figure 7** The coordination number and charge distribution of ions in $MnZrTa_2O_8$.

### *Dielectric constant $\varepsilon_r$ and bond ionicity $f_i$*

The $\varepsilon_r$ of $MnZrTa_2O_8$ ceramics, as seen from Fig. 8a, gave a good consistency with respect to relative density. Compounds with higher density generally exhibited larger $\varepsilon_r$ and vice versa. In Ref. [28], Batsanov suggested that the $\varepsilon_r$ was proportional to the $f_i$. Thus, the bond ionicity of individual bonds $\mu$ in $MnZrTa_2O_8$ ceramics was calculated as follows [29]:

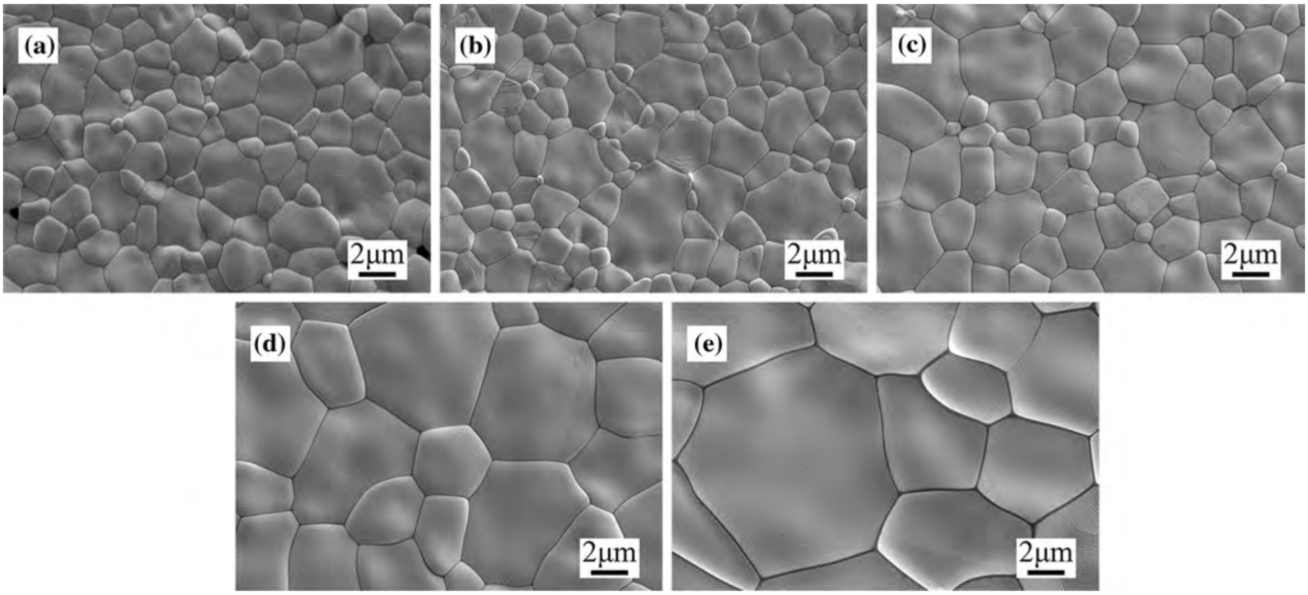

**Figure 6** SEM micrographs of $MnZrTa_2O_8$ ceramics sintered at **a** 1300 °C; **b** 1325 °C; **c** 1350 °C; **d** 1375 °C; **e** 1400 °C.

$$f_i^{\mu} = \frac{C^{\mu}}{E_g^{\mu}} \tag{6}$$

$$(E_g^{\mu})^2 = (E_h^{\mu})^2 + (C^{\mu})^2 \tag{7}$$

$$(E_h^{\mu})^2 = \frac{39.74}{(d^{u})^{2.48}} \tag{8}$$

$$C^{\mu}=14.4b^{\mu}\exp\left(-k_s^{\mu}\frac{d^{\mu}}{2}\right)\left[(Z_A^{\mu})^* - \frac{n}{m}(Z_B^{\mu})^*\right]\left(\frac{d^{\mu}}{2}\right)^{-1} \tag{9}$$

where $E_g^{\mu}$ was composed of homopolar $E_h^{\mu}$ and heteropolar $C^{\mu}$. The $(Z_A^{\mu})^*$ and $(Z_B^{\mu})^*$ were effective number of valence electrons inions, respectively. $d^{\mu}$ was the bond length. Table 5 gives the bond ionicity $f_i$ for $MnZrTa_2O_8$ ceramics sintered at 1350 °C.

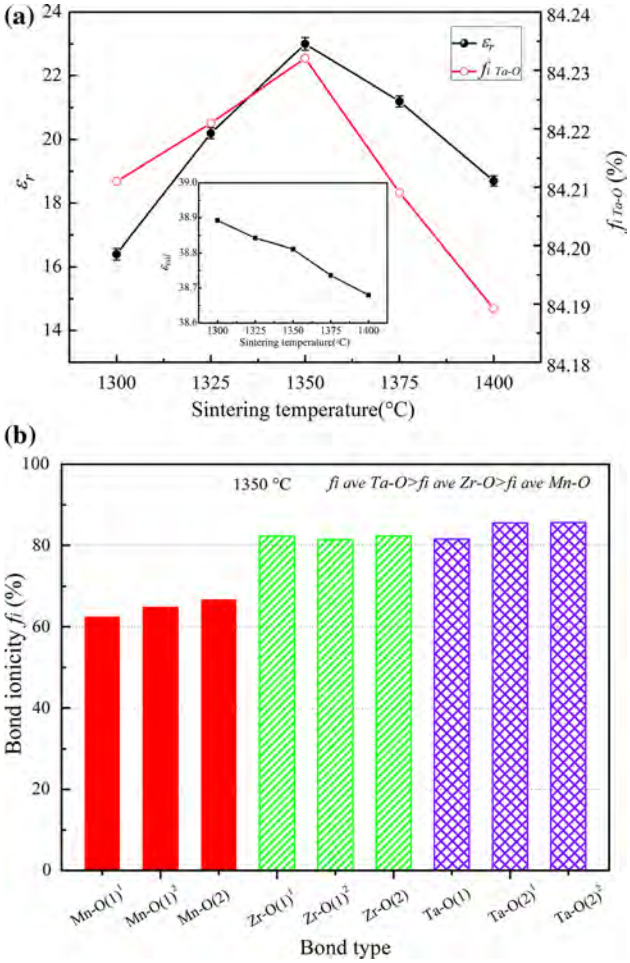

**Figure 8** **a** Dielectric constant $\varepsilon_r$ and average bond ionicity $f_i$ of Ta–O bonds for $MnZrTa_2O_8$ ceramics at different temperatures; **b** The bond ionicity $f_i$ of metal–O bonds for $MnZrTa_2O_8$ ceramics sintered at 1350 °C. The inset shows the calculated dielectric constant by Clausius–Mossotti equation.

Comparison of the results in Fig. 8b showed the sequence, i.e., Ta–O > Zr–O > Mn–O. So the Ta–O bonds might have a vital effect on the dielectric polarization behavior. With increasing temperature, the variations of $\varepsilon_r$ and average Ta-site bond ionicity are shown in Fig. 8a. From it, we could see that the smaller the ionicity, the smaller $\varepsilon_r$. The dielectric constants were estimated using the Clausius–Mossotti (C–M) equation as follows [30]:

$$\varepsilon_{cal}=\frac{3V_m + 8\pi\alpha_D}{3V_m - 4\pi\alpha_D} \tag{10}$$

where $\alpha_D$ is the total polarizability of the substance in molar volume $V_m$. The molecular polarizabilities of a certain complex could be calculated by oxide additivity rule [30]. At temperature below 1350 °C, the calculated and measured values moved in opposite directions. That was because the C–M equation was just strictly valid only for compounds with cubic symmetry. Additionally, the sample studied here was a ceramic but not a single crystal. From Fig. 8a, it was also seen that the measured values were slightly smaller than calculated. The difference arose primarily due to the ionic or electronic conductivity, the $H_2O$ or $CO_2$ in channels, and the presence of rattling or compressed cations. The dipolar impurities might be also contributed.

### *Quality factor $Q \times f$ and lattice energy $U_{cal}$*

As seen from Fig. 9, the $Q \times f$ increased steadily with temperature till 1350 °C and subsequently showed an obvious downtrend. The higher densification was believed to be the reason for the $Q \times f$ enhancement at first. Besides, the possible effect of grain boundaries acting as two-dimensional defects could not be overlooked [4]. Larger grain size stood for a decrease in the total number of grain boundaries. Hence, this long-range ordering improved the $Q \times f$. Nevertheless, this consistency between the two was destroyed after 1350 °C. It happened due to the deleterious effect brought by porous microstructure. The microwave dielectric losses generally fall into two parts: extrinsic and intrinsic [31]. The former was dominated by second phase, grain size and porosity, while the latter was related to crystal structure. The lattice energy $U_{cal}$ reflected binding ability between anions and cations. So, it was calculated in $MnZrTa_2O_8$ system based on Eqs. [32, 33]:

**Table 5** Bond ionicity $f_i$ for $MnZrTa_2O_8$ ceramics sintered at 1350 °C

| Bond type | $d$ (Å) | $E_h^2$ | $C^2$ | $E_g^2$ | $f_c$ (%) | $f_i$ (%) |
|---|---|---|---|---|---|---|
| Mn–O(1)$^1$ × 2 | 2.1871 | 32.56 | 54.23 | 86.79 | 37.5172 | 62.4828 |
| Mn–O(1)$^2$ × 2 | 2.2349 | 29.25 | 53.95 | 83.20 | 35.1563 | 64.8437 |
| Mn–O(2) × 2 | 1.7777 | 91.20 | 182.78 | 273.99 | 33.2872 | 66.7128 |
| Zr–O(1)$^1$ × 2 | 1.9742 | 54.11 | 250.91 | 305.02 | 17.7413 | 82.2587 |
| Zr–O(1)$^2$ × 2 | 2.1956 | 31.94 | 139.64 | 171.58 | 18.6161 | 81.3839 |
| Zr–O(2) × 2 | 1.8752 | 69.85 | 323.85 | 393.70 | 17.7408 | 82.2592 |
| Ta–O(1) × 2 | 2.0361 | 46.43 | 205.31 | 251.74 | 18.4441 | 81.5559 |
| Ta–O(2)$^1$ × 2 | 2.1234 | 37.70 | 223.06 | 260.76 | 14.4589 | 85.5411 |
| Ta–O(2)$^2$ × 2 | 1.8934 | 66.58 | 395.75 | 462.33 | 14.4006 | 85.5994 |
| Average $f_{i\ \text{Mn–O}}$ | | | | | | 64.6797 |
| Average $f_{i\ \text{Zr–O}}$ | | | | | | 81.9673 |
| Average $f_{i\ \text{Ta-O}}$ | | | | | | 84.2321 |

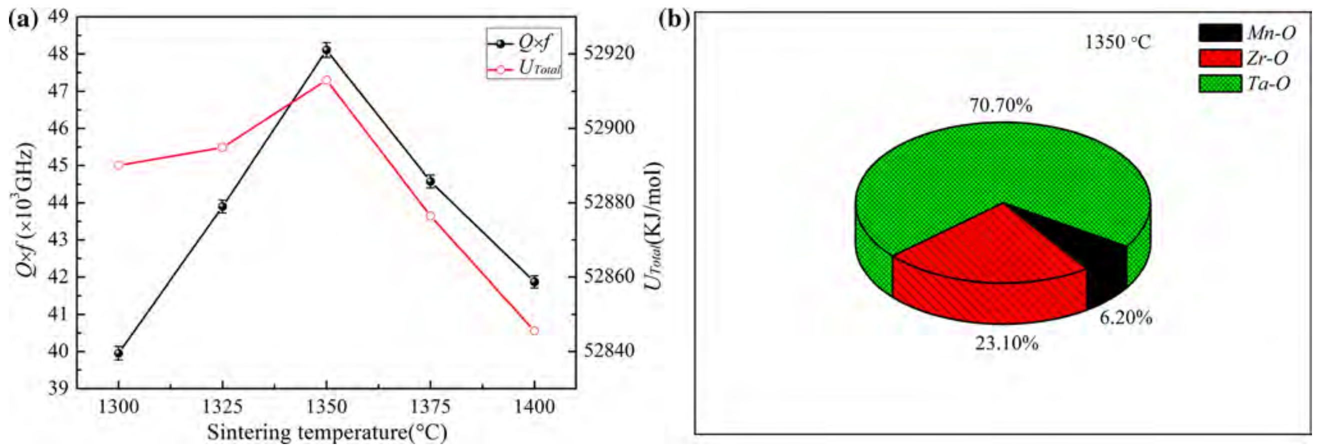

**Figure 9** **a** Quality factor $Q \times f$ and total lattice energy $U_{\text{total}}$ for $MnZrTa_2O_8$ ceramics at different temperatures; **b** contributions of metal–O bonds to the $Q \times f$ value for $MnZrTa_2O_8$ ceramics sintered at 1350 °C.

$$U_{\text{cal}} = \sum_{\mu} U_b^{\mu} \tag{11}$$

$$U_b^{\mu} = U_{bc}^{\mu} + U_{bi}^{\mu} \tag{12}$$

$$U_{bc}^{\mu} = 2100m \frac{(Z_+^{\mu})^{1.64}}{(d^{\mu})^{0.75}} f_c^{\mu} \tag{13}$$

$$U_{bi}^{\mu} = 1270m \frac{(m+n)Z_+^{\mu} Z_-^{\mu}}{d^{\mu}} \left(1 - \frac{0.4}{d^{\mu}}\right) f_i^{\mu} \tag{14}$$

where $U_{bc}^{\mu}$ and $U_{bi}^{\mu}$ were covalent and ionic lattice energy of bond $\mu$. $Z_+^{\mu}$ and $Z_-^{\mu}$ were the valence states of cation and anion. The lattice energies of $MnZrTa_2O_8$ ceramics sintered at 1350 °C are given in Table 6. The lattice energy for Mn–O, Zr–O and Ta–O bonds was 3281.59 kJ/mol, 12222.03 kJ/mol and 37409.40 kJ/mol, respectively. In particular, the Ta–O bonds made 70.70% contributions to the $Q \times f$. The total lattice energy ($U_{\text{total}}$) dependence of sintering temperature is plotted in Fig. 9a. It is noticed that $Q \times f$ and $U_{\text{total}}$ presented a similar variation tendency. Low lattice energy manifested improved lattice anharmonicity and then increased intrinsic loss [34]. It was therefore believed that there would be a deterioration in $Q \times f$ above 1350 °C. The encouraging thing was that $MnZrTa_2O_8$ yielded comparable $Q \times f$ value ~ 48103 GHz, as compared to 27936 GHz in $MnZrNb_2O_8$ [6].

## *Temperature coefficient of the resonant frequency $\tau_f$ and bond energy E*

The $\tau_f$ of $MnZrTa_2O_8$ ceramics in Fig. 10 shifted from − 50.55 to − 41.21 ppm/ °C. It was widely acknowledged that the $\tau_f$ was sensitive to structures. According to Sandderson [35, 36], the bond energy could be required from the electronegativity by:

**Table 6** Lattice energy for $MnZrTa_2O_8$ ceramics sintered at 1350 °C

| Bond type | $d$ (Å) | $f_i$ (%) | $f_c$ (%) | $U_{bc}$ (kJ/mol) | $U_{bi}$ (kJ/mol) | $U$ (kJ/mol) |
|---|---|---|---|---|---|---|
| Mn–O(1)$^1$ × 2 | 2.1871 | 62.4828 | 37.5172 | 446.69 | 593.23 | 1039.92 |
| Mn–O(1)$^2$ × 2 | 2.2349 | 64.8437 | 35.1563 | 409.63 | 605.36 | 1014.99 |
| Mn–O(2) × 2 | 1.7777 | 66.7128 | 33.2872 | 487.60 | 739.09 | 1226.69 |
| Zr–O(1)$^1$ × 2 | 1.9742 | 82.2587 | 17.7413 | 729.02 | 3401.35 | 4130.37 |
| Zr–O(1)$^2$ × 2 | 2.1956 | 81.3839 | 18.6161 | 687.84 | 3103.42 | 3791.26 |
| Zr–O(2) × 2 | 1.8752 | 82.2592 | 17.7408 | 767.49 | 3532.91 | 4300.40 |
| Ta–O(1) × 2 | 2.0361 | 81.5559 | 18.4441 | 2117.25 | 10219.47 | 12336.72 |
| Ta–O(2)$^1$ × 2 | 2.1234 | 85.5411 | 14.4589 | 1591.55 | 10381.45 | 11973.00 |
| Ta–O(2)$^2$ × 2 | 1.8934 | 85.5994 | 14.4006 | 1777.68 | 11322.00 | 13099.68 |
| $U_{Mn–O}$ | | | | | | 3281.59 |
| $U_{Zr–O}$ | | | | | | 12222.03 |
| $U_{Ta–O}$ | | | | | | 37409.40 |
| $U_{Total}$ | | | | | | 52913.02 |

$$E = \sum_{\mu} E_b^{\mu} \tag{15}$$

$$E_b^{\mu} = t_c E_c^{\mu} + t_i E_i^{\mu} \tag{16}$$

$$t_c + t_i = 1 \tag{17}$$

where $E_b^{\mu}$ was the sum of nonpolar covalence energy $E_c^{\mu}$ and complete iconicity energy $E_i^{\mu}$. The $t_c$ and $t_i$ were covalent and ionic blending coefficients, and they always satisfied Eq. (17). $E_c^{\mu}$ and $E_i^{\mu}$ could be evaluated by Eqs. (18) and (19).

$$E_i^{\mu} = \frac{33200}{d^{\mu}} \tag{18}$$

$$E_c^{\mu} = \frac{r_{cA} + r_{cB}}{d^{\mu}} (E_{A-A} E_{B-B})^{1/2} \tag{19}$$

where $r$ and $d^{\mu}$ were the covalent radii and bond length, respectively. $E_{A–A}$ and $E_{B–B}$ were the homonuclear bond energy, gained from the handbook [37]. The calculated bond energy for $MnZrTa_2O_8$ ceramics sintered at 1350 °C is displayed in Table 7. The results show that the bond energy of Ta–O bond was considerably superior to those of Zr–O and Mn–O. The average bond energy of Ta–O ($E_{Ta–O}$) for $MnZrTa_2O_8$ ceramics sintered at different temperatures, as well as $\tau_f$, is provided in Fig. 10. High bond energy did much good on the crystal structure stabilization. When bond energy increased, the tilting of the oxygen octahedron became more difficult; eventually, the system had a small $|\tau_f|$. This finding was in close agreement with the previous studies [34].

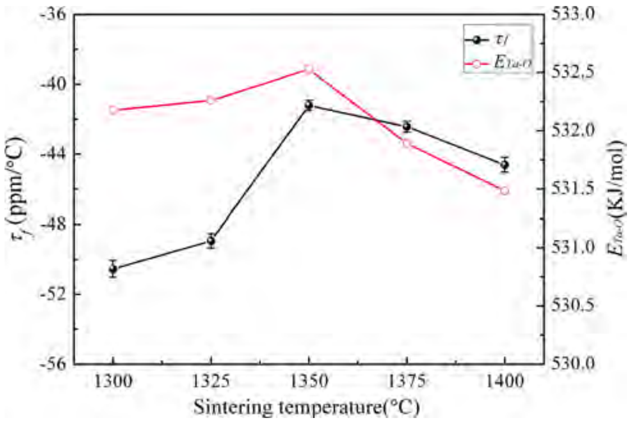

**Figure 10** Temperature coefficient of the resonant frequency $\tau_f$ and average Ta-site bond energy $E_{Ta–O}$ for $MnZrTa_2O_8$ ceramics.

## Conclusions

MnO, $Ta_2O_5$ and $ZrO_2$ were used as raw materials to synthesize $MnZrTa_2O_8$ by solid-phase method. The existence of intermediate $MnTa_2O_6$ phase was established during calcination. Single-phase $MnZrTa_2O_8$ was generated when the temperature exceeded 1200 °C. After sintering, all these compounds formed in a monoclinic structure with $P2/c$ space group. Raman spectroscopy was used to evidence the bond characteristics of samples. Both the $\varepsilon_r$ and $Q \times f$ enlarged firstly and reached the maximum value at 1350 °C and then decreased gradually. Analysis by P–V–L chemical bond theory clearly clarified the importance of Ta–O bond in affecting the dielectric properties, principally owing to its greatest bond ionicity and lattice energy. Particularly, $MnZrTa_2O_8$ ceramics were well densified at 1350 °C with a considerable enhancement in $Q \times f \sim 48103$ GHz

**Table 7** Bond energy for $MnZrTa_2O_8$ ceramics sintered at 1350 °C

| Bond type | $d$ (Å) | $S_A$ | $S_B$ | $t_i$ | $t_c$ | $E_i$ (kJ/mol) | $E_c$ (kJ/mol) | $E$ (kJ/mol) |
|---|---|---|---|---|---|---|---|---|
| Mn–O(1)$^1$ × 2 | 2.1871 | 1.55 | 3.44 | 0.3150 | 0.6850 | 635.41 | 145.80 | 300.03 |
| Mn–O(1)$^2$ × 2 | 2.2349 | 1.55 | 3.44 | 0.3150 | 0.6850 | 621.82 | 142.68 | 293.61 |
| Mn–O(2) × 2 | 1.7777 | 1.55 | 3.44 | 0.3150 | 0.6850 | 781.74 | 179.38 | 369.12 |
| Zr–O(1)$^1$ × 2 | 1.9742 | 1.33 | 3.44 | 0.3517 | 0.6483 | 703.93 | 423.73 | 522.27 |
| Zr–O(1)$^2$ × 2 | 2.1956 | 1.33 | 3.44 | 0.3517 | 0.6483 | 632.96 | 381.01 | 469.61 |
| Zr–O(2) × 2 | 1.8752 | 1.33 | 3.44 | 0.3517 | 0.6483 | 741.10 | 446.11 | 549.84 |
| Ta–O(1) × 2 | 2.0361 | 1.51 | 3.44 | 0.3217 | 0.6783 | 682.53 | 452.53 | 526.52 |
| Ta–O(2)$^1$ × 2 | 2.1234 | 1.51 | 3.44 | 0.3217 | 0.6783 | 654.47 | 433.93 | 504.87 |
| Ta–O(2)$^2$ × 2 | 1.8934 | 1.51 | 3.44 | 0.3217 | 0.6783 | 733.97 | 486.64 | 566.20 |
| Average $E_{Mn–O}$ | | | | | | | | 320.92 |
| Average $E_{Zr–O}$ | | | | | | | | 513.91 |
| Average $E_{Ta–O}$ | | | | | | | | 532.53 |

($f$ = 8.97 GHz). At the same time, the $\varepsilon_r$ and $\tau_f$ were 23.0 and − 41.21 ppm/ °C, respectively.

## Acknowledgements

This work was supported by the National Natural Science Foundation of China (51902268) and the Sichuan Science and Technology Program (2019YFG0234).

## Compliance with ethical standards

**Conflict of interest** The authors declare that they have no conflict of interest.

## References

[1] Sebastian MT (2008) Dielectric materials for wireless communications. Elsevier, Oxford

[2] Yadav P, Sinha E (2019) Structural, photophysical and microwave dielectric properties of α-$ZnMoO_4$ phosphor. J Alloys Compd 795:446–452

[3] Suresh EK, Ratheesh R (2019) Structure and microwave dielectric properties of glass free low temperature co-firable $SrMV_2O_7$ (M = Mg, Zn) ceramics. J Alloys Compd 808:151641–151648

[4] Sebastian MT, Ubic R, Jantunen H (2017) Microwave materials and applications. Wiley, Chichester

[5] Ichinose N, Shimada T (2006) Effect of grain size and secondary phase on microwave dielectric properties of $Ba(Mg_{1/3}Ta_{2/3})O_3$ and Ba $([Mg, Zn]_{1/3}Ta_{2/3})O_3$ systems. J Eur Ceram Soc 26:1755–1759

[6] Ramarao SD, Murthy VRK (2013) Crystal structure refinement and microwave dielectric properties of new low dielectric loss $AZrNb_2O_8$ (A: Mn, Zn, Mg and Co) ceramics. Scr Mater 69:274–277

[7] Tang X, Yang H, Zhang QL, Zhou JH (2014) Low-temperature sintering and microwave dielectric properties of $ZnZrNb_2O_8$ ceramics with $BaCu(B_2O_5)$ addition. Ceram Int 40:12875–12881

[8] Wu HT, Bi JX (2016) Synthesis, characterization, and microwave dielectric properties of monoclinal structure $ZnZrNb_2O_8$ ceramics through the aqueous sol-gel process. J Mater Sci: Mater Electron 27:3474–3480

[9] Wu MJ, Zhang YC, Xiang MQ (2018) Structural, Raman spectroscopic and microwave dielectric studies on $(1-x)NiZrNb_2O_8$–$xZnTa_2O_6$. J Mater Sci: Mater Electron 29:14471–14478

[10] Lyu XS, Li LX, Zhang S (2016) A new low-loss dielectric material $ZnZrTa_2O_8$ for microwave devices. J Eur Ceram Soc 36:931–935

[11] Lyu XS, Li LX, Sun H, Zhang S, Li S (2016) High-$Q$ microwave dielectrics in wolframite magnesium zirconium tantalite ceramics. Ceram Int 42:2036–2040

[12] Lin YJ, Wang SF, Lai BC, Liu YX, Chang YL, Yang JR (2017) Densification, microstructure evolution, and microwave dielectric properties of $Mg_{1-x}Ca_xZrTa_2O_8$ ceramics. J Eur Ceram Soc 37:2825–2831

[13] Zhang Y, Ding SH, Song TX (2019) Microwave dielectric properties of temperature stable MO–$ZrO_2$–$Ta_2O_5$ ceramics. J Alloys Compd 798:194–203

[14] Li EZ, Wen QY, Yang HC, Yang HY, Yang Q, Zhang SR (2019) Novel temperature stable $NiSnTa_2O_8$ microwave dielectric ceramics with trirutile structure. Ceram Int. https://doi.org/10.1016/j.ceramint.2019.11.069

[15] Chu YQ, Zhao LP, Liu Y, Liu P (2019) $MgTiTa_2O_8$: novel middle-permittivity microwave dielectric ceramic with trirutile-type structure. Ceram Int 45:23853–23856

[16] Yang HY, Zhang SR, Chen YW, Yang HC, Yuan Y, Li EZ (2019) Crystal chemistry, Raman spectra, and bond characteristics of trirutile-type $Co_{0.5}Ti_{0.5}TaO_4$ microwave dielectric ceramics. Inorg Chem 58:968–976

[17] Toby BH (2001) EXPGUI, a graphical user interface for GSAS. J Appl Cryst 34:210–213

[18] Kobayashiy Y, Katoh M (1985) Microwave measurement of dielectric properties of low-loss materials by the dielectric rod resonator method. IEEE Trans Microw Theory 33:586–592

[19] Yang HY, Zhang SR, Li YP et al (2020) Investigations of dielectric properties of wolframite $A_{0.5}Zr_{0.5}NbO_4$ ceramics by bond theory and far-infrared spectroscopy. Ceram Int 46:3688–3694

[20] Rousseau DL, Bauman RP, Porto SPS (1981) Normal mode determination in crystals. J Raman Spectrosc 10:253–290

[21] Murtaza G, Hussain SS, Rehman NU, Naseer S, Shafiq M, Zakaullah M (2011) Carburizing of zirconium using a low energy Mather type plasma focus. Surf Coat Technol 205:3012–3019

[22] Zhang H, Diao CL, Liu SL, Jiang SZ, Shi F, Jing XP (2014) X-ray diffraction and Raman scattering investigations on $Ba[Mg_{(1-x)/3}Zr_xTa_{2(1-x)/3}]O_3$ solid solutions. J Alloys Compd 587:717–723

[23] Iliev MN, Abrashev MV, Lee HG, Popov VN, Sun YY, Thomsen C, Meng RL, Chu CW (1998) Raman active phonons in orthorhombic $YMnO_3$ and $LaMnO_3$. J Phys Chem Solids 59:1982–1984

[24] Julien C, Massot M, Hadjean RB, Franger S, Bach S, Pereira-Ramos JP (2003) Raman spectra of birnessite manganese dioxides. Solid State Ionics 159:345–356

[25] Phillips JC, Van Vechten JA (1969) Dielectric classification of crystal structures, ionization potentials, and band structures. Phys Rev Lett 22:705–708

[26] Phillips J (1970) Ionicity of the chemical bond in crystals. Rev Mod Phys 42:317–356

[27] Wu ZJ, Meng QB, Zhang SY (1998) Semiempirical study on the valences of Cu and bond covalency in $Y_{1-x}Ca_xBa_{2-}Cu_3O_{6+y}$. Phys Rev B 58:958–962

[28] Batsanov SS (1982) Dielectric methods of studying the chemical bond and the concept of electronegativity. Russ Chem Rev 51:684–697

[29] Meng QB, Wu ZJ, Zhang SY (1998) Evaluation of the energy barrier distribution in many-particle systems using the path integral approach. Phys Condens Mater 10:85–88

[30] Shannon RD (1993) Dielectric polarizabilities of ions in oxides and fluorides. J Appl Phys 73:348–366

[31] Kim WS, Kim TH, Kim ES, Yoon KH (1998) Microwave dielectric properties and far reflectivity spectra of the $(Zr_{0.8}Sn_{0.2})TiO_4$ ceramics with additives. Jpn J Appl Phys 37:5367–5371

[32] Jenkins HDB, Tudela D, Glasser L (2002) Lattice potential energy estimation for complex ionic salts from density measurements. Inorg Chem 41:2364–2367

[33] Liu DT, Zhang SY, Wu ZJ (2003) Lattice energy estimation for inorganic ionic crystals. Inorg Chem 42:2465–2469

[34] Zhao YG, Zhang P (2015) Phase composition, crystal structure, complex chemical bond theory and microwave dielectric properties of high-*Q* materials in a $(Nd_{1-x}Y_x)$-$NbO_4$ system. RSC Adv 5:97746–97754

[35] Sanderson RT (1983) Electronegativity and bond energy. J Am Chem Soc 105:2259–2261

[36] Sanderson RT (1968) Multiple and single bond energies in inorganic molecules. Inorg Nucl Chem 30:375–393

[37] Luo YR (2007) Comprehensive handbook of chemical bond energies. CRC Press, Boca Raton